Block ratio optimized cationic polyacrylamides for enhanced nitrate rejection under applied potential

Hossein Vahid, Arsalan Hashemi, Mohammad Khavani, Abhinav Sharma, Mohammad R. K. Mofrad, Tapio Ala-Nissila

Angaben zur Veröffentlichung / Publication details:

Vahid, Hossein, Arsalan Hashemi, Mohammad Khavani, Abhinav Sharma, Mohammad R. K. Mofrad, and Tapio Ala-Nissila. 2025. "Block ratio optimized cationic polyacrylamides for enhanced nitrate rejection under applied potential." Chemical Engineering Journal 513: 162346. https://doi.org/10.1016/j.cej.2025.162346.

Chemical Engineering Journal 513 (2025) 162346

Contents lists available at ScienceDirect

Chemical Engineering Journal

journal homepage: www.elsevier.com/locate/cej

Block ratio optimized cationic polyacrylamides for enhanced nitrate rejection under applied potential

Hossein Vahid [a,b,1], Arsalan Hashemi [b,1], Mohammad Khavani [c], Abhinav Sharma [d], Mohammad R.K. Mofrad [c,e,*], Tapio Ala-Nissila [b,f,g,**]

[a] Leibniz-Institut für Polymerforschung Dresden, Institut Theorie der Polymere, 01069 Dresden, Germany
[b] Department of Applied Physics, Aalto University, P.O. Box 15600, FI-00076 Aalto, Finland
[c] Molecular Cell Biomechanics Laboratory, Departments of Bioengineering and Mechanical Engineering, University of California Berkeley, Berkeley, CA, USA
[d] Faculty of Mathematics, Natural Sciences, and Materials Engineering: Institute of Physics, University of Augsburg, Universitätsstraße 1, 86159 Augsburg, Germany
[e] Molecular Biophysics and Integrative Bioimaging Division, Lawrence Berkeley National Laboratory, Berkeley, CA, USA
[f] Quantum Technology Finland Center of Excellence, Department of Applied Physics, Aalto University, P.O. Box 15600, FI-00076, Aalto, Finland
[g] Interdisciplinary Centre for Mathematical Modelling and Department of Mathematical Sciences, Loughborough University, Loughborough, Leicestershire LE11 3TU, United Kingdom

ARTICLE INFO

Dataset link: https://doi.org/10.5281/zenodo.15263666

Keywords:
Polyacrylamide
Water purification
Reverse osmosis
Membrane
Molecular dynamics simulation
Sodium nitrite

ABSTRACT

Nitrate contamination in water sources is a growing environmental concern, threatening both human health and ecosystems. However, its combination with sodium forms $NaNO_3$, a compound essential for various industrial applications. The integration of charged polymers and reverse osmosis (RO) membranes presents a promising approach to capture undesired ions and enhance water purification efficiency. In this paper, diblock cationic polyacrylamides (DCPAMs) as charged polymers are evaluated separately in bulk solution and in combination with the RO process to capture nitrite ions introduced by $NaNO_3$. Molecular dynamics simulations are conducted to systematically investigate the effects of polymer block ratio and concentration, as well as salt concentration, on NO_3^- capturing. Our results in bulk solution indicate that an optimal block ratio of 8:12 yields the highest performance, with polymers adopting a stretched conformation. When an electric potential is applied, anions are strongly attracted to the positively charged electrode, and nitrate ions remain closer to the electrode surface than other ions. Our findings reveal that a 12:8 ratio outperforms all other ratios. The simultaneous application of RO membranes and DCPAMs achieves salt rejection efficiencies ranging from 78% to 100%, depending on DCPAM type and salt concentration. These findings pave the way for further computational studies on combined processes to advance water purification technologies.

1. Introduction

Sodium nitrate ($NaNO_3$) is an important inorganic compound with wide industrial use, notably as a fertilizer [1], in thermal storage systems [2–4] and manufacturing processes [5–8]. Its extensive demand, particularly in agriculture, has led to nitrate becoming a common pollutant in water resources. Excess nitrate in groundwater and surface water is a serious environmental and public health concern [9]. In aquatic ecosystems, high nitrate levels from fertilizer runoff fuel algal blooms that deplete oxygen, causing eutrophication and ecosystem damage [10,11]. For humans, drinking water with nitrate above regulatory limits (10 $mg.L^{-1}$) can impair the blood oxygen-carrying capacity (methemoglobinemia, or blue baby syndrome in infants) and has been linked to elevated risks of certain cancers [9,12].

Various techniques have been developed to remove nitrate from water, each with practical limitations [13]. Ion exchange is a well-established method capable of achieving very low nitrate levels, but it is often hindered by non-selectivity due to resins favoring other anions, like sulfate, and generates nitrate-rich brine requiring disposal [14,15]. Biological denitrification converts NO_3^- ions to harmless nitrogen gas effectively, especially in wastewater, but demands careful process control, carbon sources, and risks introducing microbial byproducts, complicating its use in drinking water treatment [16–19]. Electrochemical reduction provides a direct conversion route to nitrogen gas or

* Corresponding author at: Molecular Cell Biomechanics Laboratory, Departments of Bioengineering and Mechanical Engineering, University of California Berkeley, Berkeley, CA, USA.
** Corresponding author at: Department of Applied Physics, Aalto University, P.O. Box 15600, FI-00076 Aalto, Finland.
E-mail addresses: mofrad@berkeley.edu (M.R.K. Mofrad), tapio.ala-nissila@aalto.fi (T. Ala-Nissila).
[1] These authors contributed equally to this work.

https://doi.org/10.1016/j.cej.2025.162346
Received 20 January 2025; Received in revised form 28 March 2025; Accepted 4 April 2025
Available online 18 April 2025

other nitrogen-contained species [13]. However, incomplete selectivity can yield unwanted byproducts such as ammonia or sludge, necessitating optimized operating conditions [9]. Adsorption methods employing activated carbon or biochar can efficiently capture NO_3^- but typically exhibit limited capacities, requiring frequent regeneration or replacement [20]. Other processes, such as electrodialysis and distillation, can remove nitrates as well, but they tend to be energy-intensive and are usually employed only when overall desalination is needed [21,22].

Pressure-driven membrane separation, particularly reverse osmosis (RO), is widely adopted for salt and nitrate removal from water due to its capability to simultaneously remove multiple contaminants [23–25]. However, conventional RO systems indiscriminately remove all salts, making them energy-intensive and inefficient when nitrate is the primary target contaminant. Current challenges, including high operational pressure and membrane fouling, drive ongoing research towards optimizing RO performance through innovative hybrid strategies [26]. Hybridizing RO with electrostatic ion removal methods presents a promising route for improving nitrate selectivity and energy efficiency [27,28]. Capacitive deionization (CDI), an emerging method employing electric potentials to adsorb ions onto charged electrodes [29–32], selectively removes contaminants with relatively low energy input, especially beneficial for moderately saline waters [28, 33–36]. The RO process commonly employs carbon-based materials, particularly graphene, as membranes. This preference can be attributed to their well-established fabrication methods, high permeability, exceptional mechanical properties, low-friction water interactions, and excellent conductivity [26,37–39]. Moreover, nanoporous graphene membranes were shown to maintain their mechanical integrity in RO [40].

Integrating ion-selective polymers into RO systems is another next-generation strategy to enhance selectivity. Charged polymers enable selective ion capture through salt dissociation and association reactions [41,42]. The idea is to incorporate a polymer that has a strong affinity for the target ion (nitrate in this case) so that the polymer acts as a supplemental ion-capture medium within or near the membrane. This integration could occur as a coating, a composite layer, or a draw solution in a hybrid process. Recent work highlights that charged polymers can indeed augment membrane purification—for instance, the coupling of cationic polymers with filtration has achieved high nitrate rejections by binding NO_3^- ions and preventing their passage [43]. Therefore, a hybrid system that leverages both RO filtration and electrostatic polymer adsorption under an applied potential is an attractive approach to address the limitations of standalone RO or CDI.

Among various ion-selective polymers, *cationic polyacrylamides* (CPAMs) are particularly promising for nitrate removal. CPAMs, water-soluble derivatives of polyacrylamide with positively charged groups such as quaternary ammonium moieties, have long been employed in water treatment as flocculants, effectively binding anions and facilitating contaminant removal [41,44–48]. It is typically a microblock structure, where modifying the functional groups of each block helps to adjust its physicochemical properties [49]. Recent studies demonstrated substantial nitrate removal (> 80%) in CPAM-assisted filtration processes compared to negligible rejection without polymer addition [43]. Moreover, the integration of CPAMs with pressurized vertical electro-osmotic dewatering has been shown to improve water removal from sludge significantly [31]. Strong electrostatic repulsion within the structure extends the molecular chain, enhancing ion accessibility to the charged segments and thereby increasing ion adsorption [41,50, 51]. Notably, the block ratio (i.e., the ratio between the number of monomers in each block) directly impacts the polymer performance, where, for instance, a high charge density can induce repulsion and destabilization [41]. Therefore, selecting the right block ratio is critical to achieving higher efficiency [52–55]. Compared with traditional ion-exchange resins, CPAMs offer advantages such as easy in situ integration into membranes as coatings or composite layers, the potential for regeneration via electrical methods, and reduced waste generation. While multiple polymer candidates exhibit selective anion-binding capabilities, such as poly(diallyldimethylammonium chloride) [41], Epichlorohydrin-Dimethylamine Polymers [41], cationic cellulose betainate [56], and Moringa oleifera seed extract [57], CPAM is selected in this study as a representative example due to proven efficiency, widespread availability, industrial applicability, cost efficiency and non-toxicity [41,45–48].

Despite extensive studies on polyelectrolyte behavior in solution, atomic-scale optimization of block ratios in CPAMs for selective anion adsorption remains largely unexplored. In this work, we address this gap by systematically tuning the ratio of charged to neutral monomers in di-block CPAMs and evaluating their adsorption efficiency for NO_3^- ions. Using molecular dynamics (MD) simulations, we demonstrate how changes in polymer architecture drastically affect ion selectivity, polymer conformation, and local ion distribution in bulk solution. Previously, polyacrylamide derivatives were shown to become more coiled as the concentration of NaCl or $CaCl_2$ salt increases [58,59]. We then integrate these optimized CPAMs into an RO-capacitive hybrid setup under a constant electric potential. Most computational studies in desalination systems have relied on idealized constant electric fields [29,30,32,60–63]. To our knowledge, this is the first study to apply constant-potential MD to such systems, capturing key features of desalination processes. We show that combining pressure-driven RO filtration, polymer-mediated ion adsorption, and electrostatic attraction enables highly selective nitrate rejection, achieving up to 100% salt removal. Overall, this study presents a systematic approach to addressing complex solution systems to improve the water purification process.

2. Simulation methods

2.1. Bulk electrolyte using GROMACS

This subsection provides details on the equilibrium MD (EMD) simulations. The EMD calculations are performed using the GROMACS package [64,65], chosen for its computational efficiency and robust performance in bulk solution calculations.

Depending on the type of the second monomer paired with acrylamide, di-block cationic polyacrylamides (DCPAMs) exhibit varying levels of toxicity, degradability, and performance [66–70]. In this study, we utilize methylated dimethyl-aminoethyl acrylate as the second monomer in the polymer, chemically referred to as *poly(acrylamide-[2-(methacryloyloxy)ethyl] trimethylammonium)*, due to its non-toxicity, slow degradability, and straightforward synthesis process [71,72]. This polymer has also been widely utilized in wastewater treatment [41,73, 74]. Henceforth, we refer to this polymer as DCPAM.

Each DCPAM chain consists of a neutral hydrophilic block with m monomers and a charged block with n monomers, denoted as A_m and B_n, respectively. Its chemical structure is shown in Fig. 1(a) . To model different block sizes, a chain of total of 20 monomers with a block ratio of m:n is used, where $m = 20 - n$. Since the B_n-block is positively charged, n numbers of Cl^- counterions per DCPAM chain are added to neutralize each polymer. We explore varying DCPAM concentrations of 5, 10, and 15 wt% by including 5, 10, and 15 DCPAMs per simulation box, respectively.

The model systems also include $NaNO_3$ as added salt and water molecules to complete the solution model. Initial solvation is performed using the GROMACS solvate tool. Three different salt concentrations, c^s = 0.1, 0.3, and 0.5 M, respectively, corresponding to 30, 90, and 150 Na^+ and NO_3^- ion pairs are also examined. The number of water molecules varies between 1.4×10^4 and 1.6×10^4, depending on the concentrations of DCPAM and $NaNO_3$.

The initial configurations are prepared by randomly distributing polymers, ions, and water molecules within an $8 \times 8 \times 8$ nm^3 cubic simulation box using Packmol [75]; see Fig. 1(b). The DCPAM chains are modeled using the OPLS-AA force field [76,77], while water molecules are represented by the TIP3P model [78]. This water model is selected due to its ability to reproduce water dielectric constant more accurately than other similar water models [79] and its compatibility with the polymer force field. All bonds in water molecules and DCPAMs are constrained using the SETTLE [80] and LINCS [81] algorithms, respectively. The interaction parameters for the Na^+ and Cl^- ions are adopted from Refs. [82,83]. The parameter for the NO_3^- ion is taken from Ref. [84].

Periodic boundary conditions are applied in all three directions. A cutoff radius of 1 nm is applied for van der Waals (vdW) potential to account for the dispersive interactions between all species in the model system. Long-range electrostatic interactions are treated using the Particle Mesh Ewald method [85] with a real-space cutoff of 1 nm. The simulations are performed with a time step of 2 fs.

All systems are first subjected to energy minimization using the steepest descent method, followed by a 10 ns equilibration in the NpT ensemble. During equilibration, the geometries of the DCPAMs are restrained, and the water molecules and ions are allowed to move freely. Temperature and pressure are controlled at $T = 298$ K and $p = 1$ bar using the velocity-rescale thermostat [86] and the cell-rescale barostat [87], with coupling constants $\tau = 0.1$ ps and $\tau = 2$ ps, respectively. Production simulations are then performed for 130 ns in the NpT ensemble but different Parrinello–Rahman barostat [88]. Trajectories are recorded every 4 ps, with the last 100 ns extracted for data analysis (25000 trajectories). The configurations are visualized using the VMD [89] and OVITO [90] packages.

2.2. Confined electrolyte using LAMMPS

This subsection provides details on the non-equilibrium MD (NEMD) simulations. The NEMD simulations are performed using the LAMMPS package [91], selected for suitability in modeling capacitive systems and non-equilibrium processes.

The final configurations of the bulk electrolyte solutions (from Section 2.1) are placed between two graphene monolayers, which form the feed reservoir. One of these layers functions as a membrane, while the other acts as a piston; see Fig. 1(c). These layers also function as electrodes, with an external potential difference applied between them. The positive electrode is on the left side of the feed reservoir, and the negative electrode is on the right. The rigid graphene layers are oriented parallel to the xy plane, with the layer at $z = -0.3$ nm acting as a piston and the one at $z = 8.3$ nm acting as the nanoporous graphene membrane. Note that an initial 0.3 nm gap between the solution and the solid surface, corresponding to the first hydration layer on carbon materials [92], facilitates the equilibration process.

The membrane contains four pores, each 1 nm in diameter, with the centers of the pores positioned 3 nm apart. The ion rejection is influenced by both the shape and size of the pores [93–95]. Pores with diameters of approximately 1 nm allow optimal water passage and salt rejection [96–98]. However, as this study does not focus on membrane optimization, the pore geometry used has been previously validated in other studies [96–101]. Moreover, the even distribution of four pores in an 8×8 nm^2 graphene sheet provides sufficient spacing between pores, allowing high water permeability without compromising the mechanical integrity of the sheet [102]. However, in-depth exploration of the membrane topology is beyond the scope of this study. An additional fixed, rigid graphene monolayer (the third layer) is positioned at $z = 18.3$ nm, defining the permeate reservoir as the region between this graphene layer and the membrane. A total of 7000 water molecules are included in the permeate reservoir to mitigate the effects of solid–liquid–gas interactions [103]. The mobile piston moves along the z axis from $z = -0.3$ to apply compression to the feed. This process continues until half of the water is transferred from the feed to the permeate. However, it is noteworthy that variations in the size and number of pores in the membrane affect the computational time required to achieve the passage of 50% water molecules.

Simulations are carried out in the NVT ensemble with a time step of 1 fs. Three independent simulations are performed for each system, and the reported values are an average of them. Before opening the pores, the systems are equilibrated for 2 ns. Subsequently, the pores are opened, and an electric potential difference of $\Delta\phi = 2$ V is applied between the piston and the membrane using the constant potential method [104], as implemented in LAMMPS. As the piston moves, the applied electric field ranges from 0.23 to 0.46 V/nm, consistent with values commonly used in nanoscale water desalination simulations [32,105,106]. As reported in Ref. [107], an applied electric field corresponding to $\Delta\phi = 2$ V achieves both high water flux through the membrane and effective salt rejection. The rigid piston moves at a velocity of $v = 1$ m/s, a commonly used value in similar studies [107,108] to minimize effects on the atomistic dynamics in the system. To estimate the equivalent loading pressure on the piston, we performed additional simulations using a constant-pressure piston instead of a constant-velocity one, for the case with five 8:12 DCPAM chains at $c^s = 0.1$ M. Our results showed that the piston velocity of 1 m/s used in our NEMD runs corresponds to a pressure of about 15 MPa, which is a standard practice in similar MD studies [109–111]. The trajectory analyses are performed after the production simulations have run for about 4–5 ns, during which half of the water molecules are transferred from the feed container to the permeate reservoir.

Furthermore, the atomic charges of the electrodes follow a Gaussian distribution with a width of 19.79 nm^{-1}, as detailed in Ref. [112]. Long-range electrostatic interactions are calculated using the Particle–Particle Particle–Mesh (PPPM) method [113,114] with slab corrections applied along the z-axis [115,116]. The PPPM algorithm employs a dimensionless relative force accuracy of 10^{-4}, and a slab factor of 3. The temperature is maintained at $T = 298$ K using the Nosé–Hoover thermostat [117,118] with $\tau = 0.1$ ps. The same force field described in Section 2.1 is used for the DCPAM, water molecules, and ions. The vdW interaction parameters for C atoms of graphene are taken from Ref. [119].

3. Results and discussion

The following subsections present the findings and analysis of the correlation between block ratio, polymer concentration, and salt density, both in a homogeneous bulk solution and under the influence of an electric potential in a RO-capacitive process.

3.1. Bulk solutions

We begin by evaluating the impact of polymer architecture on anion adsorption in bulk solutions. To this end, the ion condensation around DCPAM is also examined for varying block ratios m:n.

Fig. 2(a) shows the radial distribution functions (RDF) for NO_3^-, Cl^-, Na^+ ions, and the oxygen atom of water (OW), relative to the charged groups of DCPAMs, specifically the nitrogen (N^+) ions of the B_n-block, where $n = 8$. The analysis is carried out at an added salt concentration of 0.1 M, with 5 DCPAM chains solvated. In other words, the system under consideration consists of 30 Na^+, 30 NO_3^-, and 60 Cl^- ions.

The RDF curves show distinct behaviors: (i) The peaks for OW, NO_3^-, and Cl^- ions are at $r \approx 0.46$, 0.464, and 0.494 nm, respectively, while Na^+ ions are notably absent within this region. For NO_3^- ions, the distance is calculated relative to the nitrogen atom at the center of the ion, which is symmetrically surrounded by three oxygen atoms (see Fig. 1(a)). The attraction of NO_3^- and Cl^- ions to positively charged sites on the DCPAM chains is attributed to Coulombic interactions. The differences between peak height for NO_3^- and Cl^- arise from the normalization of each curve to the number density of the respective species. This suggests that for a similar distribution of NO_3^- and Cl^-, the peak height of Cl^- should theoretically be half that of NO_3^-. However, the highest RDF peak height of NO_3^- (≈ 19) is more than twice that of Cl^- (≈ 5.8), suggesting stronger adsorption of NO_3^- to the B-blocks. (ii)

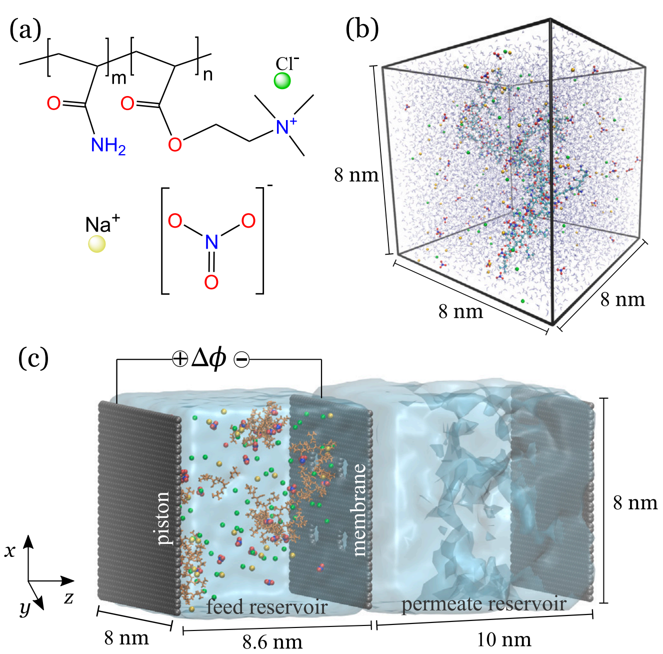

Fig. 1. (a) The chemical structure of A_mB_n di-block cationic polyacrylamide and $NaNO_3{}^-$. The DCPAM has m neutral and n charged monomers, accompanied by n Cl^- counterions. (b) Snapshot of a simulation box after 130 ns in the NpT ensemble. The box consists of 5 chains of DCPAM with 12:8 block ratio, 40 Cl^- counterions, 0.1 M of $NaNO_3$ salt, solvated in water. (c) A representative snapshot of the RO process simulations: The DCPAMs are in orange, and the carbon atoms of graphene are in gray. The Na, Cl, N, O elements are represented by yellow, green, blue, and red colors, respectively. The feed reservoir is at $\Delta\phi = 2$ V. The positive electrode is located on the left side of the feed (piston), and the negative electrode is on the right side (membrane). (For interpretation of the references to color in this figure legend, the reader is referred to the web version of this article.)

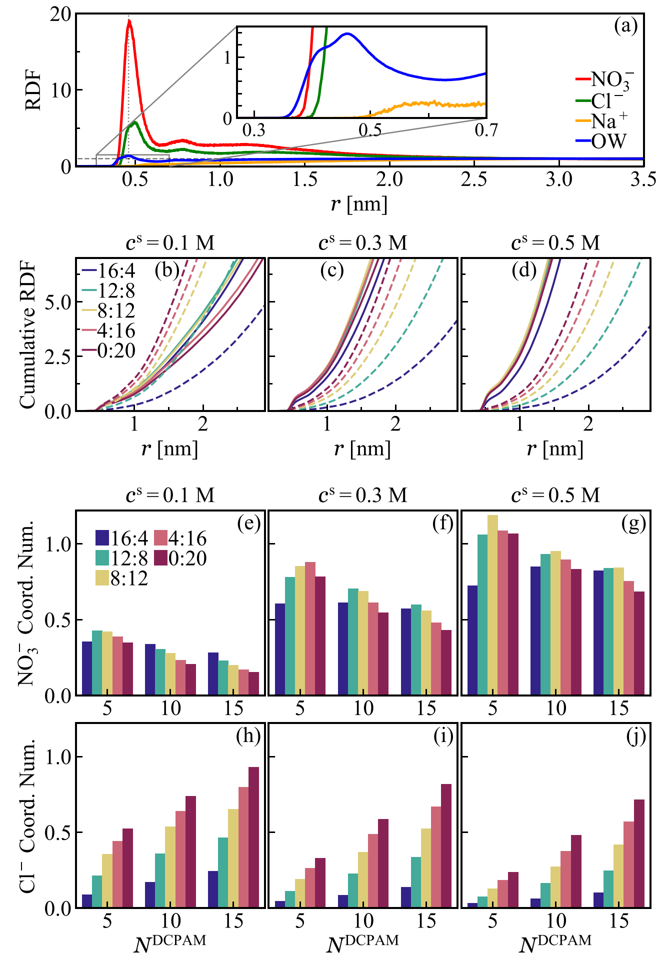

Fig. 2. (a) The radial distribution function (RDF) of various ions and water (OW) are analyzed for the block ratio of 8:12 with 5 DCPAMs, where the salt concentration is $c^s = 0.1$ M. The N^+ species of the $-N^+(CH_3)_3$ group is regarded as the reference atom. The vertical and horizontal lines correspond to $x = 0.46$ nm and $y = 1$, respectively. (b)–(d) The averaged cumulative RDF of NO_3^- (solid lines) and Cl^- (dashed lines) around the nitrogen atoms (per N^+ species) in B_n-block for varying m:n ratios and different $NaNO_3$ concentrations (c^s) at $N^{DCPAM} = 5$. Both RDF and cumulative RDF are in dimensionless units (see the SM for definitions). (e)–(g) The coordination number of NO_3^-, and (h)–(j) the coordination number of Cl^-, are determined from $n(r)$ using a cutoff distance of $r_{cut} = 0.66$ nm for varying $NaNO_3$ concentrations.

A secondary peak accompanied by a satellite curve extends to 2 nm, representing longer-range electrostatic correlations. In this region, Na^+ ions are also present, but their density remains lower than NO_3^- and Cl^- ions. (iii) The dipolar water molecules orient their negatively charged oxygen atoms towards the nitrogen atom of the B-block, forming stable hydration shells, regardless of the m:n ratio and salt concentration (see Fig. S1 of Supplementary Material (SM)). This interaction induces notable clustering of water molecules around the polymer; however, it is weaker than direct ion-polymer Coulomb interactions, leading to RDF peaks that are lower than those of the anions, yet still appreciable. (iv) The Na^+ ions, being positively charged, experience electrostatic repulsion from the positively charged polymer segments. As a result, they are depleted in the vicinity of the B-block nitrogen atoms, and their RDF gradually approaches the bulk value at larger r.

The distribution of NO_3^- and Cl^- ions for varying numbers of DCPAM molecules (N^{DCPAM}) and c^s are presented in Figs. S2 and S3 of the SM. NO_3^- ions are predominantly localized at a distance of about 0.46 nm from the N^+ sites of the $-N^+(CH_3)_3$ groups, accompanied by minor peaks in the longer-range regions. Cl^- ions exhibit a similar trend, but their main peak is shorter and broader, reflecting weaker and less localized interactions. Furthermore, as c^s increases, the density of Cl^- ions close to the N^+ atoms of B-block decreases, indicating competitive interactions between NO_3^- and Cl^- ions.

Quantum mechanical calculations summarized in Sect. SIII of SM reveal that the ionic bonds in NaCl are stronger than those in $NaNO_3$ (see Fig. S4). This finding supports the hypothesis that $NaNO_3$ dissociates in solution, allowing the Na^+ and Cl^- ions to attract each other, while the NO_3^- ions remain more freely mobile. These observations are consistent with the lower solubility of NaCl as compared to $NaNO_3$, as previously reported in Ref. [120]. Subsequently, the NO_3^- ions can be attracted to the DCPAMs. Additionally, our findings are consistent with the Hofmeister series, which predicts that NO_3^- associates with positively charged nitrogen in $-N^+(CH_3)_3$, while Cl^- favors Na^+ ions [121].

To explore the effect of the block ratio m:n on anion adsorption at different concentrations of $NaNO_3$, we calculated time-averaged cumulative RDFs of NO_3^- and Cl^- ions (see Figs. 2(b)–(d)). At the lowest salt concentration, $c^s = 0.1$ M and for $n \leq 8$, where the number of Cl^- ions (< 40 ions) is comparable to the number of NO_3^- ions (30 ions), NO_3^- ions exhibit stronger adsorption to the polymers than Cl^- ions. However, for $n > 8$, the number of Cl^- ions exceeds that of NO_3^- ions, and the cumulative RDF of Cl^- becomes larger, indicating a shift in adsorption preference. At higher salt concentrations ($c^s = 0.3$ and 0.5 M), the number of NO_3^- ions is approximately equal to or greater than the number of Cl^- ions, resulting in a greater fraction of NO_3^- ions adsorbed near the polymer chains as compared to Cl^- ions.

To better understand the impact of the m:n ratio, we also examine the effect of varying the number of DCPAM chains (see Fig. S5 of SM). Our results reveal that as the NO_3^-/Cl^- number ratio increases, a more pronounced shoulder emerges in the cumulative RDF of NO_3^- ions at $r < 0.66$ nm, indicating a denser distribution in this region. Moreover, the m:n ratio plays a crucial role in the adsorption competition between

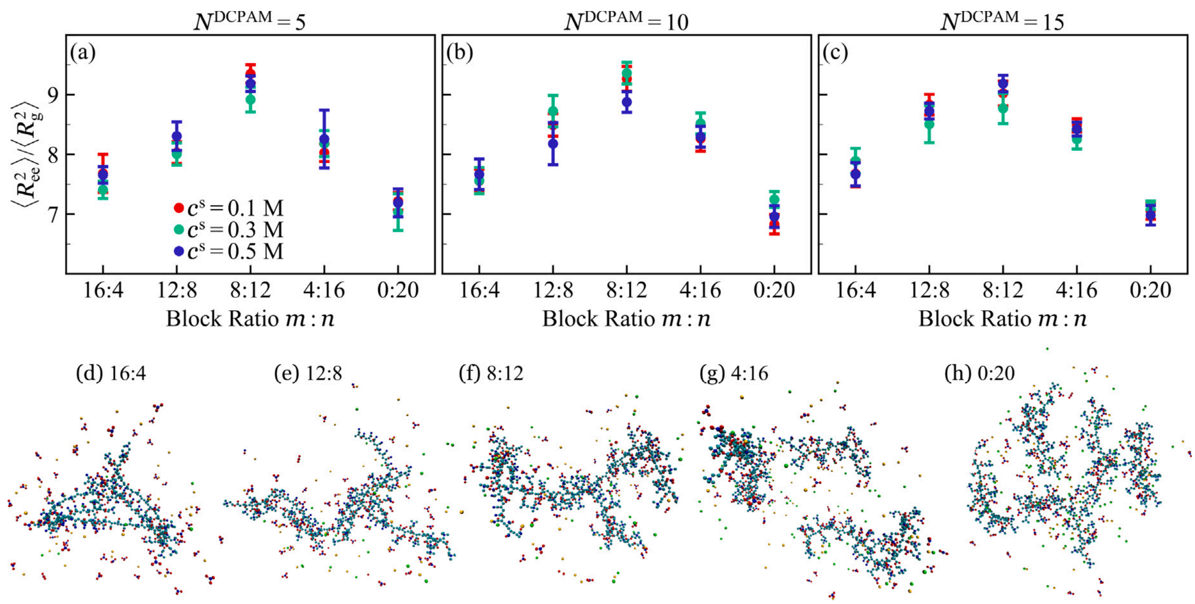

Fig. 3. The ratio between mean-square end-to-end distance ($\langle R_{\mathrm{ee}}^2 \rangle$) and mean-square radius ($\langle R_{\mathrm{g}}^2 \rangle$) of gyration of DCPAMs as a function of block ratio m:n. The results are presented for three different added salt concentrations c_{s} = 0.1, 0.3, and 0.5 M, as well as three different DCPAM concentrations of (a) 5, (b) 10, and (c) 15 wt%. Panels (d)–(h) depict the structural conformation of copolyelectrolytes in the presence of 0.1 M $NaNO_3$ salt, for c_{DCPAM} = 5 wt%, after 130 ns of NpT simulation. The atoms are represented using the same color scheme as depicted in Fig. 1, with H atoms excluded for enhancing clarity.

the ions when it can change the relative balance between the number of NO_3^- and Cl^- ions in the system.

We compare the NO_3^- and Cl^- coordination numbers at a distance of 0.66 nm from the nitrogen of $-N^+(CH_3)_3$ group under various conditions, as shown in Figs. 2(e)–(j). The results indicate that at a fixed salt concentration c^{s}, increasing the concentration of DCPAMs consistently reduces the average number of NO_3^- ions adsorbed per nitrogen atom in the B-block. In contrast, Cl^- ions exhibit the opposite trend. Moreover, as the salt concentration increases in a fixed m:n ratio, the polymers coordinate more NO_3^- ions, displacing Cl^- ions into the bulk solution. For example, at c^{s} = 0.5 M (150 NO_3^- ions) and for $n > 8$, each B-block, on average, adsorbs one NO_3^- ion, resulting in the near-complete exclusion of Cl^- ions in the vicinity of B-block N^+ atoms. This is further confirmed by the Cl^- coordination numbers, which decrease systematically with increasing salt concentration.

To further investigate the conformation of DCPAMs in the solution, we calculated $\langle R_{\mathrm{ee}}^2 \rangle / \langle R_{\mathrm{g}}^2 \rangle$. Here, $\langle R_{\mathrm{ee}}^2 \rangle$ represents the mean-squared distance between the two terminal points of a polymer chain in a given configuration, while $\langle R_{\mathrm{g}}^2 \rangle$ denotes the mean-squared distance of the polymer's monomers from the polymer's center of mass. This ratio quantitatively reflects chain conformations: higher values correspond to more extended chains, with values above 6 indicating coil-like structures and values below 6 representing collapsed chains [122–124].

Figs. 3(a)–(c) illustrate that the conformations remain relatively unaffected by changing salt concentrations from 0.1 M to 0.5 M. This stability suggests that the electrostatic screening effects introduced by the added salt do not significantly influence the chain conformations under the conditions studied. However, the block ratio m:n has a pronounced effect on the chain conformation. Among the tested configurations, the 8:12 DCPAM exhibits the highest $\langle R_{\mathrm{ee}}^2 \rangle / \langle R_{\mathrm{g}}^2 \rangle$, indicating that these chains are more stretched compared to those with other block ratios. This finding highlights that the 8:12 configuration achieves an optimal balance between charged group electrostatic repulsion and the uncharged blocks (A-block) flexibility. As a result, the less compact conformation enhances the accessibility and binding of ions.

Interestingly, varying the number of DCPAM chains N^{DCPAM} from 5 to 15 has little impact on chain conformations, as indicated by the nearly constant $\langle R_{\mathrm{ee}}^2 \rangle / \langle R_{\mathrm{g}}^2 \rangle$ values. This invariance implies that chain conformations are primarily dictated by intra-chain interactions rather than inter-chain effects or crowding within the studied concentration range. These findings highlight that the chain architecture, particularly the block ratio m:n, exerts the most significant influence on chain conformation, outweighing external factors such as salt and polymer concentrations.

Panels (d)–(h) of Fig. 3 illustrate the configuration of chains with varying block ratios m:n for c^{s} = 0.1 M when N^{DCPAM} = 5. As n increases, the total charge of the polymer increases correspondingly, enhancing the electrostatic repulsion between chains within the simulation box. This enhanced repulsion increases the spacing between chains, reducing the probability of aggregation between chains. Notably, the 16:4 DCPAM chains exhibit a strong tendency to aggregate, clustering into a single cohesive structure. This behavior is due to the reduced charge density in the B-block, which weakens the electrostatic repulsion between chains and allows hydrophobic interactions to dominate, facilitating aggregation. In contrast, the 0:20 CPAM chains, which consist entirely of the charged monomers, remain completely separated. The high polymer charge in this configuration maximizes electrostatic repulsion, preventing aggregation and maintaining well-dispersed chain conformations. These analyses further indicate the critical role of block architecture in the balance between electrostatic and hydrophobic interactions. Similar trends have been reported in Ref. [58].

3.2. Confined solutions

We now turn to the results of the confined model under a constant potential difference. For this, different conformational DCPAM species were placed between the positively charged piston and the negatively charged membrane in the presence of 0.1 M $NaNO_3$. The models contain five polymers.

Fig. 4 illustrates that the simultaneous application of potential and variations in the m:n ratio have distinct effects on ion separation and, consequently, on filtration efficiency. However, the membrane's negative total charge attracts the DCPAM chains to its surface. In contrast, anions can become close to the membrane surface or the polymers, depending on the abundance of positive monomers (i.e., m:n ratio).

Clearly, as n increases, a systematic exchange of NO_3^- and Cl^- densities on the piston wall can be found, with NO_3^- remaining closer

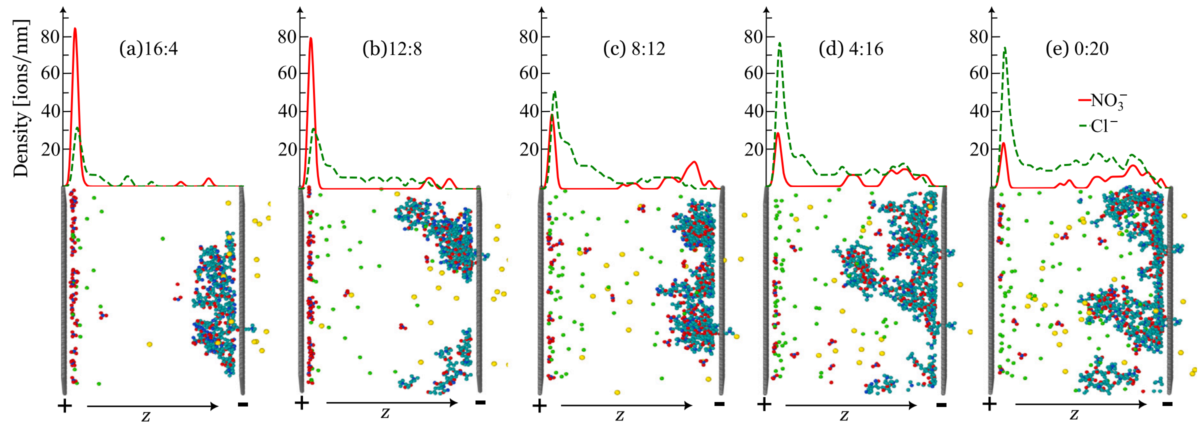

Fig. 4. The structural conformation of CDPAMs, with different block ratios m:n between piston (+) and membrane (−) surfaces in the presence of 0.1 M $NaNO_3$ salt solution after 2 ns. The models contain five polymers. An electric potential difference of $\Delta\phi = +2$ V is imposed between layers, leading to negative and positive net charges on the membrane and piston surfaces, respectively. The atoms are represented using the same color scheme as depicted in Fig. 1, with H atoms excluded for enhanced clarity. The densities of NO_3^- ions (red solid line) and Cl^- ions (green dashed line) are represented for each case. (For interpretation of the references to color in this figure legend, the reader is referred to the web version of this article.)

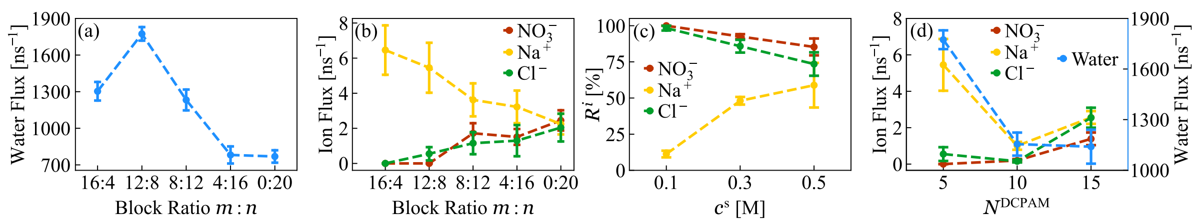

Fig. 5. (a) Water and (b) ion fluxes passing through membrane pores as a function of block ratio m:n in $NaNO_3$ salt. In these cases, $N^{DCPAM} = 5$ and $c^s = 0.1$ M. (c) The ion rejection R^i (Eq. (2)) as a function of $NaNO_3$ concentration, where the DCPAM block ratio is 12:8. This model contains five polymers. Error bars represent the variability across three independent initial feed configurations extracted from the final 30 ns of the corresponding bulk solution simulations. (d) Ion fluxes (left) and water fluxes (right) as a function of the number of DCPAM chains N^{DCPAM} at a fixed salt concentration of $c^s = 0.1$ M and a DCPAM block ratio of 12:8. Dashed lines are guides to the eyes.

to the wall as compared to Cl^- ions. During this transition, NO_3^- ions are attracted to the polymers and become localized on the B-blocks, while Cl^- ions are distributed throughout the solution, with higher intensity near the piston wall. The schematics also show that Na^+ ions are more populated in the feed reservoir in the presence of higher Cl^- levels (higher n) and are less transferred into the permeate. Indeed, this behavior can be attributed to the blockage of membrane pores by adsorbed molecules. Polymer coverage of the membrane surface can reduce the degradation rate caused by chlorination, which is a major limitation of membranes.

Flux of species i through the membrane, Flux^i, is calculated at the time when half of the water molecules are transferred from the feed to the permeate reservoir ($t_{1/2}$). It is formulated as

$$\text{Flux}^i = \frac{N^i_{\text{trans}}(t = t_{1/2})}{t_{1/2}}, \tag{1}$$

where $N^i_{\text{trans}}(t = t_{1/2})$ indicates the number of i transported from feed to permeate at the time of $t_{1/2}$.

Figs. 5(a)–(b) depict the water and ion fluxes through the membrane for varying block ratios m:n. We observe that the total number of water molecules that traverse the membrane pores per unit of time is the highest for the 12:8 CPAM system. Beyond a B_n-block ratio of $n = 8$, a significant reduction in water flux is observed, primarily due to the increased obstruction of the pore area caused by higher polymer density. Recent studies have reported maximum water fluxes of 600 ns^{-1} and 140 ns^{-1} from nanoporous graphene membranes [32] and boron nitride membranes [30], respectively. However, as shown in Fig. 5(a), the presence of four nanopores in the graphene system studied here leads to a substantial increase in water flux, reaching values as high as 1800 ns^{-1}.

According to the ion flux data in Fig. 5(b), we find that by increasing the B_n-block ratio, the flux of NO_3^- and Cl^- ions increases from 0 to roughly 2.2 ns^{-1}, whereas the flux of Na^+ ions decreases. In the 0:20 DCPAM system, the flux of Na^+ ions reaches a minimum value of approximately 2.2 ns^{-1}, which is one-third of the flux observed in the 16:4 system. Notably, in the 12:8 case, where the water flux is maximum, none of the NO_3^- ions pass through the membrane, and the Cl^- flux is relatively small.

To explore the effect of salt concentration on the flow of ions, we calculate the ion rejection parameter. Ion rejection (R) rate for ion type i is defined as [125]

$$R^i = \left(1 - \frac{N^i_{\text{trans.}}(t = t_{1/2})}{N^i_{\text{feed}}(t = 0)}\right) \times 100 \tag{2}$$

where $N^i_{\text{feed}}(t = 0)$ is the initial number of ions of type i in the feed side.

In Fig. 5(c), we compare R for different ion types. It shows that at $c^s = 0.1$ M, $R \approx 100\%$ for the anions, inhibiting most of these ions from entering the permeate reservoir. In general, the rejection of anions decreases to 78% as the salt concentration increases to $c^s = 0.5$ M, although most of the Na^+ ions can pass through the membrane at all salt concentrations. This phenomenon is natural because $-N^+(CH_3)_3$ cannot accommodate all anions. Consequently, some anions form stronger attractions to the Na^+ ions, keeping them confined to the feed reservoir.

Fig. 5(d) illustrates the trade-off between water permeability and ion selectivity as influenced by the number of polymer chains (N^{DCPAM}). As the polymer concentration increases, the partial obstruction of the nanopores is enhanced, resulting in a physical hindrance and reduction of water and Na^+ ions fluxes. However, since the number of Cl^- ions in the system increases as N^{DCPAM} increases, the passage of anions from the pores slightly increases. Such permeability–selectivity trade–offs have also been widely documented in RO membranes literature, emphasizing the critical challenge of balancing contaminant rejection with water throughput [126,127].

While the impact of electric field application on the RO process has been extensively demonstrated [29–32], we further examined ion rejection in the absence of polymers. Our results indicate that the rejection rate R is comparable to that observed at low DCPAM concentrations, with higher R values reflecting greater efficiency (cf. Fig. S6). However, the influence of polymer concentration across different block ratios remains unclear and warrants further investigation. In addition to ion rejection, system stability is a critical consideration; polymers are introduced not only to enhance rejection performance but also to improve stability by mitigating undesired side effects [9,43].

4. Conclusions

This study demonstrates the significant potential of integrating charged polymers with RO membranes to enhance water purification by effectively capturing and excluding undesired ions. Specifically, DCPAMs were systematically evaluated in both bulk solutions and under RO-capacitive conditions to target NO_3^- ions introduced by $NaNO_3$ salt.

Using MD simulations, the study explored the effects of polymer configuration, concentration, and salt concentration on ion adsorption and system performance. The results revealed that NO_3^- ions exhibit strong adsorption to the charged polymers, displacing Cl^- ions into the bulk solution. Importantly, polymer configuration emerged as a critical determinant of performance, with optimal configurations enhancing ion selectivity and adsorption efficiency. As the concentration of the polymer and the concentration of the salt varied, the results demonstrated that system-specific polymer properties could achieve a delicate balance between NO_3^- ion adsorption and Cl^- ion exclusion. The NEMD model employed a constant electric potential (instead of a uniform field) to mimic an applied voltage bias. Under the application of an electric potential, anions were strongly attracted to the positive electrode, with NO_3^- ions preferentially remaining closer to the surface. This selective ion behavior, combined with the filtration capabilities of the RO membrane, enabled salt rejection efficiencies ranging from 78% to 100%, demonstrating the significant enhancements achievable through hybrid systems.

These findings not only validate the efficacy of combining charged polymers with RO membranes but also emphasize the importance of polymer architecture and operating conditions in optimizing water purification performance. The study provides a robust computational framework for investigating the dynamic interactions in such systems and sets the stage for future research to refine and scale these technologies.

While experimental work is beyond the scope of this study, we identify several viable techniques to validate our findings. These include zeta potential and conductivity measurements to probe polymer-ion interactions, quartz crystal microbalance studies to examine polymer adsorption on membranes or electrode surfaces, and dead-end filtration experiments using polymer-modified membranes to evaluate nitrate rejection, water flux, and fouling behavior [128]. These approaches can directly test simulation-derived hypotheses and support practical implementation. Moreover, bridging the nanoscale results to engineering-scale applications requires a multi-scale modeling approach. Coupling MD with continuum theories or computational fluid dynamics simulations can help capture flow dynamics, membrane polarization, and large-scale behavior [129]. Furthermore, progressive bench-scale testing, starting with small membrane patches and scaling to larger RO modules, can validate and refine performance predictions [130,131].

Although our study has shown the significant role of polymer on NO_3^- removal and its molecular mechanism, some questions/deficiencies remain that can be explored in future investigations: (i) Our model simplifies the membrane as rigid graphene layers. Future work can consider flexible membranes, which may exhibit different structural and electrostatic responses, potentially affecting polymer adsorption and ion transport. (ii) The influence of functional group modifications and counterion selection in DCPAMs deserves further exploration. These parameters can significantly affect polymer solubility, chain conformation, and ion-binding behavior, as well as contribute to secondary salt formation, especially near charged interfaces like the piston. (iii) Grafting polymers onto membrane or piston surfaces could enhance ion-capturing efficiency and mitigate fouling, thereby improving long-term operational stability. Future studies can explore the effectiveness of such surface-grafted systems under applied pressure and electric fields to assess desalination performance. (iv) Advancing membrane engineering efforts to optimize pore geometry, such as tuning pore shape and size, can help balance ion rejection and water permeability, ultimately contributing to more efficient and sustainable operation.

CRediT authorship contribution statement

Hossein Vahid: Writing – original draft, Visualization, Validation, Software, Methodology, Investigation, Formal analysis, Data curation, Conceptualization. **Arsalan Hashemi:** Writing – original draft, Visualization, Validation, Software, Methodology, Investigation, Formal analysis, Data curation, Conceptualization. **Mohammad Khavani:** Writing – review & editing, Conceptualization. **Abhinav Sharma:** Writing – review & editing, Resources, Funding acquisition. **Mohammad R.K. Mofrad:** Writing – review & editing, Supervision, Resources, Funding acquisition. **Tapio Ala-Nissila:** Writing – review & editing, Supervision, Resources, Funding acquisition.

Declaration of competing interest

The authors declare that they have no known competing financial interests or personal relationships that could have appeared to influence the work reported in this paper.

Acknowledgments

The Finnish Cultural Foundation, Finland supported this work under grant no. 00241182 (H. V.). A. H. and T. A-N. have been supported by the Academy of Finland, Finland through its QTF Center of Excellence program (Project No. 312298). The Academy of Finland, Finland also supported the work under the European Union – NextGenerationEU instrument by the Academy of Finland grant 353298 (T. A-N.). The work was further supported by the Technology Industries of Finland Centennial Foundation, Finland TT2020 grant (T. A-N.). Computational resources by the CSC IT Centre for Finland and the Aalto Science-IT are also gratefully acknowledged.

Appendix A. Supplementary data

Supplementary material related to this article can be found online at https://doi.org/10.1016/j.cej.2025.162346.

Data availability

Link to the inputs of the simulations and data is provided at https://doi.org/10.5281/zenodo.15263666.

References

[1] S.M. Yahaya, A.A. Mahmud, M. Abdullahi, A. Haruna, Pedosphere 33 (3) (2023) 385–406.
[2] A. Lomonaco, D. Haillot, E. Pernot, E. Franquet, J.-P. Bedecarrats, ECOS 2015-the 28th International Conference on Efficiency, Cost, Optimization, Simulation and Environmental Impact of Energy Systems, 2015.
[3] G. Xu, G. Leng, C. Yang, Y. Qin, Y. Wu, H. Chen, L. Cong, Y. Ding, Sol. Energy 146 (2017) 494–502.
[4] V. Hari Suthan, K. Suganthi, K. Rajan, Sci. Rep. 14 (1) (2024) 23619.
[5] N. Andenan, W.M.Z. Wan Yunus, M.N. Norrrahim, N.S. Abdul Latif, H. Ariff, R. Jamian, N.A. Salleh, N.F. Abdul Rahman, Z. Salleh, K.A. Ahmad, et al., Def. S T Tech. Bull. 17 (2) (2024).

[6] EFSA Panel on Food Additives and Nutrient Sources added to Food (ANS), A. Mortensen, F. Aguilar, R. Crebelli, A. Di Domenico, B. Dusemund, M.J. Frutos, P. Galtier, D. Gott, U. Gundert-Remy, et al., EFSA J. 15 (6) (2017) e04787.
[7] M.F. Dewan, M.N. Islam, M.S. Azam, Food Safety, CRC Press, Boca Raton, 2024, pp. 155–184.
[8] J. Shi, J. Xu, X. Liu, A.A. Goda, S.H. Salem, M.M. Deabes, M.I. Ibrahim, K. Naguib, S.R. Mohamed, Discov. Food 4 (1) (2024) 89.
[9] J. Wang, F. Sharaf, A. Kanwal, Env. Sci. Pollut. Res. Int. 30 (4) (2023) 9290–9310.
[10] W.A. Wurtsbaugh, H.W. Paerl, W.K. Dodds, Wiley Interdiscip. Rev. Water 6 (5) (2019) e1373.
[11] M.J. Brush, M. Giani, C. Totti, J.M. Testa, J. Faganeli, N. Ogrinc, W.M. Kemp, S.F. Umani, Coast. Ecosyst. Transit.: A Comp. Anal. North. Adriat. Chesap. Bay (2020) 75–104.
[12] M.H. Ward, R.R. Jones, J.D. Brender, T.M. De Kok, P.J. Weyer, B.T. Nolan, C.M. Villanueva, S.G. Van Breda, Int. J. Env. Res. Public Heal. 15 (7) (2018) 1557.
[13] H.M.A. El-Lateef, M.M. Khalaf, A.E.-d. Al-Fengary, M. Elrouby, Molecules 27 (8) (2022) 2552.
[14] B.-U. Bae, Y.-H. Jung, W.-W. Han, H.-S. Shin, Water Res. 36 (13) (2002) 3330–3340.
[15] S. Sharifian, N.-H.L. Wang, J. Env. Chem. Eng. (2024) 112402.
[16] H. Lu, K. Chandran, D. Stensel, Water Res. 64 (2014) 237–254.
[17] Y. Jin, M.C. Veiga, C. Kennes, J. Chem. Technol. Biotechnol. 80 (5) (2005) 483–494.
[18] F. Rezvani, M.-H. Sarrafzadeh, S. Ebrahimi, H.-M. Oh, Env. Sci. Pollut. Res. 26 (2019) 1124–1141.
[19] V.B. Jensen, J.L. Darby, C. Seidel, C. Gorman, Crit. Rev. Environ. Sci. Technol. 44 (20) (2014) 2203–2286.
[20] M. Choudhary, M. Muduli, S. Ray, Sustain. Water Resour. Manag. 8 (4) (2022) 113.
[21] S.M.J.S. Sabour, B. Ghorashi, Sep. Purif. Technol. (2024) 127913.
[22] P. Xu, T.Y. Cath, A.P. Robertson, M. Reinhard, J.O. Leckie, J.E. Drewes, Env. Eng. Sci 30 (8) (2013) 502–514.
[23] L. Wang, T. Cao, J.E. Dykstra, S. Porada, P. Biesheuvel, M. Elimelech, Environ. Sci. Technol. 55 (24) (2021) 16665–16675.
[24] D.T. Nguyen, S. Lee, K.P. Lopez, J. Lee, A.P. Straub, Sci. Adv. 9 (28) (2023) eadg6638.
[25] S. Bolisetty, R. Mezzenga, Nat. Nanotechnol. 11 (4) (2016) 365–371.
[26] S. Wu, L.E. Peng, Z. Yang, P. Sarkar, M. Barboiu, C.Y. Tang, A.G. Fane, Nanomicro Lett. 17 (1) (2025) 1–24.
[27] N. Ghaffour, T.M. Missimer, G.L. Amy, Desalination 309 (2013) 197–207.
[28] P. Srimuk, X. Su, J. Yoon, D. Aurbach, V. Presser, Nat. Rev. Mater. 5 (7) (2020) 517–538.
[29] H. Gao, Q. Shi, D. Rao, Y. Zhang, J. Su, Y. Liu, Y. Wang, K. Deng, R. Lu, J. Phys. Chem. C 121 (40) (2017) 22105–22113.
[30] H. Gao, Q. Shi, P. Král, R. Lu, J. Phys. Chem. C 123 (45) (2019) 27690–27696.
[31] Z. Cao, V. Liu, A. Barati Farimani, Nano Lett. 19 (12) (2019) 8638–8643.
[32] H. Gao, Q. Xu, J. Wang, C. Ning, Y. Liu, Y. Xie, R. Lu, J. Phys. Chem. Lett. 13 (1) (2022) 258–266.
[33] M. Metzger, M.M. Besli, S. Kuppan, S. Hellstrom, S. Kim, E. Sebti, C.V. Subban, J. Christensen, Energy Env. Sci. 13 (6) (2020) 1544–1560.
[34] S. Porada, R. Zhao, A. van der Wal, V. Presser, P.M. Biesheuvel, Prog. Mater. Sci. 58 (8) (2013) 1388–1442.
[35] Y. Xiong, F. Yu, S. Arnold, L. Wang, V. Presser, Y. Ren, J. Ma, Research (2021).
[36] Q. Shi, K. Zhang, R. Lu, J. Jiang, J. Membr. Sci. 545 (2018) 49–56.
[37] T. Liu, J. Lyv, Y. Xu, C. Zheng, Y. Liu, R. Fu, L. Liang, J. Wu, Z. Zhang, Desalination 533 (2022) 115775.
[38] D.J. Johnson, N. Hilal, Desalination 500 (2021) 114852.
[39] S. Castelletto, A. Boretti, RSC Adv. 11 (2021) 7981–8002.
[40] D. Cohen-Tanugi, J.C. Grossman, Nano Lett. 14 (11) (2014) 6171–6178.
[41] E.M. Wilts, J. Herzberger, T.E. Long, Polym. Int. 67 (7) (2018) 799–814.
[42] M.F. Ahmer, M.K. Uddin, RSC Adv. 14 (2024) 33629–33648.
[43] X. Li, L. He, X. Liao, Y. Song, C. Huang, K. Luo, Y. Pang, IOP Conference Series: Earth and Environmental Science, vol. 781, (no. 5) IOP Publishing, 2021, 052030.
[44] Z. Cheng, Z. Dong, M. Su, Y. Zhang, Z. Wang, P. He, J. Macromol. Sci 56 (1) (2019) 76–85.
[45] V. Vajihinejad, R. Guillermo, J.B. Soares, Ind. Eng. Chem. Res. 56 (5) (2017) 1256–1266.
[46] Y. Liu, D. Zhang, B. Ren, X. Gong, A. Liu, Y. Chang, Y. He, J. Zheng, Langmuir 36 (11) (2020) 2757–2766.
[47] W. Li, R.K. Saini, J. Macromol. Sci. 58 (4) (2020) 243–248.
[48] C. Ferrag, S. Li, K. Jeon, N.M. Andoy, R.M.A. Sullan, S. Mikhaylichenko, K. Kerman, Colloids Surf. B Biointerfaces 197 (2021) 111397.
[49] Y. Chen, X. Li, W. Zizeng, L. Feng, J. Xie, Z. Lin, Z. Xu, B. Liu, X. Li, H. Zheng, Env. Sci. Pollut. Res. 28 (2021) 51865–51878.
[50] Y. Chen, L. Feng, B. Liu, J. Peng, Y. Chen, C. Xu, J. Ren, J. Appl. Polym. Sci. 137 (46) (2020) 49519.
[51] B. Bolto, J. Gregory, Water Res. 41 (11) (2007) 2301–2324.
[52] Y. Zhou, H. Zheng, B. Gao, Y. Gu, X. Li, B. Liu, A.M. Jiménez, RSC Adv. 7 (2017) 28733–28745.
[53] Y. Guo, Y. Liang, X. Yang, R. Feng, R. Song, J. Zhou, F. Gao, J. Appl. Polym. Sci. 131 (16) (2014).
[54] M.G. Rasteiro, F.A.P. Garcia, P.J. Ferreira, E. Antunes, D. Hunkeler, C. Wandrey, J. Appl. Polym. Sci. 116 (6) (2010) 3603–3612.
[55] F.N. Ajjan, M. Ambrogi, G.A. Tiruye, D. Cordella, A.M. Fernandes, K. Grygiel, M. Isik, N. Patil, L. Porcarelli, G. Rocasalbas, G. Vendramientto, E. Zeglio, M. Antonietti, C. Detrembleur, O. Inganäs, C. Jérôme, R. Marcilla, D. Mecerreyes, M. Moreno, D. Taton, N. Solin, J. Yuan, Polym. Int. 66 (8) (2017) 1119–1128.
[56] K. Sievänen, J. Kavakka, P. Hirsilä, P. Vainio, K. Karisalmi, J. Fiskari, I. Kilpeläinen, Cellulose 22 (2015) 1861–1872.
[57] B. García-Fayos, J. Arnal, L. Monforte-Monleon, M. Sancho, Desalin. Water Treat. 55 (13) (2015) 3635–3645.
[58] P. Chen, L. Yao, Y. Liu, J. Luo, G. Zhou, B. Jiang, J. Mol. Model. 18 (2012) 3153–3160.
[59] S. Yang, T. Ma, Y. He, X. Su, AIP Adv. 11 (3) (2021) 035032.
[60] A. Zapata-Sierra, M. Cascajares, A. Alcayde, F. Manzano-Agugliaro, Desalination 519 (2021) 115305.
[61] L. Zhang, X. Kan, T. Huang, J. Lao, K. Luo, J. Gao, X. Liu, K. Sui, L. Jiang, Water Res. 219 (2022) 118598.
[62] D. Curto, V. Franzitta, A. Guercio, Appl. Sci. 11 (2) (2021) 670.
[63] L. Lin, W. Jiang, X. Xu, P. Xu, Npj Clean Water 3 (1) (2020) 25.
[64] M.J. Abraham, T. Murtola, R. Schulz, S. Páll, J.C. Smith, B. Hess, E. Lindahl, SoftwareX 1–2 (2015) 19–25.
[65] S. Páll, M.J. Abraham, C. Kutzner, B. Hess, E. Lindahl, in: S. Markidis, E. Laure (Eds.), Solving Software Challenges for Exascale, Springer International Publishing, Cham, 2015, pp. 3–27.
[66] B. Zakaria Djibrine, H. Zheng, M. Wang, S. Liu, X. Tang, S. Khan, A.N. Jimenéz, L. Feng, Int. J. Polym. Sci. 2018 (1) (2018) 5294251.
[67] L. Feng, H. Zheng, B. Gao, C. Zhao, S. Zhang, N. Chen, RSC Adv. 7 (2017) 11626–11635.
[68] Y. Liao, H. Zheng, L. Qian, Y. Sun, L. Dai, W. Xue, Ind. Eng. Chem. Res. 53 (27) (2014) 11193–11203.
[69] Z. Zhang, H. Zheng, F. Huang, X. Li, S. He, C. Zhao, Ind. Eng. Chem. Res. 55 (37) (2016) 9819–9828.
[70] B. Gao, Y. Lv, H. Jiu, Polym. Int. 52 (9) (2003) 1468–1473.
[71] A. Steudel, F. Friedrich, W. Lieske, W. Baille, D. König, R. Schuhmann, K. Emmerich, Heliyon 5 (12) (2019).
[72] D. Hennecke, A. Bauer, M. Herrchen, E. Wischerhoff, F. Gores, Env. Sci. Eur. 30 (2018) 1–13.
[73] D.V. Morales, B.L. Rivas, N. Escalona, Polym. Bull. 73 (2016) 875–890.
[74] D.I. Al-Risheq, M.S. Nasser, H. Qiblawey, M.M. Ba-Abbad, A. Benamor, I.A. Hussein, J. Water Process. Eng. 40 (2021) 101885.
[75] L. Martínez, R. Andrade, E.G. Birgin, J.M. Martínez, J. Comput. Chem. 30 (13) (2009) 2157–2164.
[76] W.L. Jorgensen, J. Tirado-Rives, J. Am. Chem. Soc. 110 (6) (1988) 1657–1666.
[77] W.L. Jorgensen, J. Gao, J. Phys. Chem. 90 (10) (1986) 2174–2182.
[78] W.L. Jorgensen, J. Chandrasekhar, J.D. Madura, R.W. Impey, M.L. Klein, J. Chem. Phys. 79 (2) (1983) 926–935.
[79] C. Vega, J.L. Abascal, M. Conde, J. Aragones, Faraday Discuss. 141 (2009) 251–276.
[80] S. Miyamoto, P.A. Kollman, J. Comput. Chem. 13 (8) (1992) 952–962.
[81] B. Hess, H. Bekker, H.J. Berendsen, J.G. Fraaije, J. Comput. Chem. 18 (12) (1997) 1463–1472.
[82] J. Aqvist, J. Phys. Chem. 94 (21) (1990) 8021–8024.
[83] J. Chandrasekhar, D.C. Spellmeyer, W.L. Jorgensen, J. Am. Chem. Soc. 106 (4) (1984) 903–910.
[84] B. Doherty, X. Zhong, S. Gathiaka, B. Li, O. Acevedo, J. Chem. Theory Comput. 13 (12) (2017) 6131–6145.
[85] U. Essmann, L. Perera, M.L. Berkowitz, T. Darden, H. Lee, L.G. Pedersen, J. Chem. Phys. 103 (19) (1995) 8577–8593.
[86] G. Bussi, D. Donadio, M. Parrinello, J. Chem. Phys. 126 (1) (2007) 014101.
[87] M. Bernetti, G. Bussi, J. Chem. Phys. 153 (11) (2020) 114107.
[88] M. Parrinello, A. Rahman, J. Appl. Phys. 52 (12) (1981) 7182–7190.
[89] W. Humphrey, A. Dalke, K. Schulten, J. Mol. Graph. 14 (1996) 33–38.
[90] A. Stukowski, Modelling Simul. Mater. Sci. Eng. 18 (1) (2009) 015012.
[91] A.P. Thompson, H.M. Aktulga, R. Berger, D.S. Bolintineanu, W.M. Brown, P.S. Crozier, P.J. in't Veld, A. Kohlmeyer, S.G. Moore, T.D. Nguyen, et al., Comput. Phys. Comm. 271 (2022) 108171.
[92] A. Akaishi, T. Yonemaru, J. Nakamura, ACS Omega 2 (5) (2017) 2184–2190.
[93] M. Heiranian, A.B. Farimani, N.R. Aluru, Nat. Commun. 6 (1) (2015) 8616.
[94] M.-Y. Huang, Q. Lyu, S.-C. Chien, L.-C. Lin, J. Phys. Chem. C 127 (44) (2023) 21740–21748.
[95] M. Raju, P.B. Govindaraju, A.C.T. van Duin, M. Ihme, Nanoscale 10 (2018) 3969–3980.
[96] S.P. Surwade, S.N. Smirnov, I.V. Vlassiouk, R.R. Unocic, G.M. Veith, S. Dai, S.M. Mahurin, Nat. Nanotechnol. 10 (5) (2015) 459–464.
[97] D. Cohen-Tanugi, J.C. Grossman, Nano Lett. 12 (7) (2012) 3602–3608.
[98] D. Cohen-Tanugi, J.C. Grossman, J. Chem. Phys. 141 (7) (2014) 074704.

[99] L. Wang, J. He, M. Heiranian, H. Fan, L. Song, Y. Li, M. Elimelech, Sci. Adv. 9 (15) (2023) eadf8488.

[100] T. Fujioka, N. Oshima, R. Suzuki, W.E. Price, L.D. Nghiem, J. Membr. Sci. 486 (2015) 106–118.

[101] S.H. Kim, S.-Y. Kwak, T. Suzuki, Environ. Sci. Technol. 39 (6) (2005) 1764–1770.

[102] J. Yoon, M.H. Kwon, D.H. Shin, S.W. Lee, Curr. Appl. Phys. 23 (2021) 30–35.

[103] L. Garnier, A. Szymczyk, P. Malfreyt, A. Ghoufi, J. Phys. Chem. Lett. 7 (17) (2016) 3371–3376.

[104] L.J. Ahrens-Iwers, M. Janssen, S.R. Tee, R.H. Meißner, J. Chem. Phys. 157 (2022) 084801.

[105] M.K. Kandezi, M.S. Lakmehsari, C.F. Matta, J. Mol. Liq. 302 (2020) 112574.

[106] J. Azamat, J. Phys. Chem. C 120 (41) (2016) 23883–23891.

[107] A. Lohrasebi, S. Rikhtehgaran, Nano Res. 11 (2018) 2229–2236.

[108] N. Razmara, A. Kirch, J.R. Meneghini, C.R. Miranda, Energies 14 (9) (2021) 2488.

[109] G. Lin, J. Manuel Perez-Aguilar, Z. Gu, J. Mol. Liq. 383 (2023) 122054.

[110] S. He, W. Zhang, Z. Gu, Desalination 563 (2023) 116751.

[111] Y. Lu, S. Guzman, M. Rizwan, K.R. Hinkle, Z. Gu, Langmuir 41 (3) (2025) 1921–1926, PMID: 39815823.

[112] Z. Wang, Y. Yang, D.L. Olmsted, M. Asta, B.B. Laird, J. Chem. Phys. 141 (18) (2014) 184102.

[113] S. Plimpton, R. Pollock, M. Stevens, in Proceedings of the Eighth SIAM Conference on Parallel Processing for Scientific Computing, SIAM, Minneapolis, 1997.

[114] L.J. Ahrens-Iwers, R.H. Meißner, J. Chem. Phys. 155 (2021) 104104.

[115] I.-C. Yeh, M.L. Berkowitz, J. Chem. Phys. 111 (7) (1999) 3155–3162.

[116] S.R. Tee, D.J. Searles, J. Chem. Phys. 156 (18) (2022) 184101.

[117] S. Nosé, Mol. Phys. 52 (2) (1984) 255–268.

[118] W.G. Hoover, Phys. Rev. A 31 (3) (1985) 1695.

[119] R. Saito, R. Matsuo, T. Kimura, G. Dresselhaus, M. Dresselhaus, Chem. Phys. Lett. 348 (3–4) (2001) 187–193.

[120] J.G. Reynolds, ACS Omega 3 (11) (2018) 15149–15157.

[121] T. Oncsik, G. Trefalt, M. Borkovec, I. Szilagyi, Langmuir 31 (13) (2015) 3799–3807.

[122] P. Cifra, I. Teraoka, Polymer 43 (8) (2002) 2409–2415.

[123] D.G. Mintis, V.G. Mavrantzas, Macromolecules 53 (18) (2020) 7618–7634.

[124] H. Huo, W. Zhao, X. Duan, Z.-Y. Sun, Macromolecules 56 (3) (2023) 1065–1076.

[125] D. Cohen-Tanugi, L.-C. Lin, J.C. Grossman, Nano Lett. 16 (2) (2016) 1027–1033.

[126] F. Zhang, Z. Zhang, Z. Liu, G. Cheng, S. Li, J. Ding, Desalination 546 (2023) 116182.

[127] Z. Zhang, S. Li, B. Mi, J. Wang, J. Ding, Sci. Adv. 6 (34) (2020) eaba9471.

[128] Y. Ju, J. Zhang, Q. Cai, Z. Zhang, Y. Zhao, J. Cui, R. Hou, Y. Wei, Z. Liang, F. Chen, Chem. Eng. J. 453 (2023) 139969.

[129] S. Soukane, H. Elcik, A. Alpatova, J. Orfi, E. Ali, H. AlAnsary, N. Ghaffour, J. Clean. Prod. 287 (2021) 125555.

[130] B. Mi, Science 364 (6445) (2019) 1033–1034.

[131] Y. Yang, X. Yang, L. Liang, Y. Gao, H. Cheng, X. Li, M. Zou, R. Ma, Q. Yuan, X. Duan, Science 364 (6445) (2019) 1057–1062.